Enabling Both High Efficiency and High Stability for Low-Bandgap Mixed Tin-Lead Iodide Perovskite Solar Cells

Chongwen Li¹, Zhaoning Song^{1*}, Cong Chen¹, Chuanxiao Xiao², Biwas Subedi¹, Steve P. Harvey², Niraj Shrestha¹, Kamala Khanal Subedi¹, Lei Chen¹, Dachang Liu¹, You Li¹, Yongwah Kim³, Chun-sheng Jiang², Michael J. Heben¹, Dewei Zhao¹, Randy J. Ellingson¹, Nikolas J. Podraza¹, Mowafak Al-Jassim², and Yanfa Yan^{1*}

Abstract:

High-performance perovskite/perovskite tandem solar cells require high-efficiency and stable low-bandgap perovskite subcells. The current state-of-the-art low-bandgap mixed tin-lead iodide perovskite solar cells (PSCs) exhibit either high power conversion efficiency (PCE) or high stability, but not both. Here, we report a two-step bilayer interdiffusion growth (BIG) process to simultaneously meet both requirements for formamidinium-based low-bandgap mixed tin-lead iodide PSCs. The BIG process allows for the formation of high-quality and large grained perovskite films with only 10 mol% volatile methylammonium. Additionally, one-dimensional pyrrolidinium perovskite is applied to passivate the perovskite film and improve the junction quality, resulting in a carrier lifetime of 1.1 µs and an open circuit voltage of 0.865 V for our 1.28-eV bandgap perovskite film and device. Our strategies enable a PCE of 20.4% for low-bandgap PSCs under AM1.5 illumination. More importantly, an encapsulated device can retain 92% of its initial efficiency after 450 hours of continuous one sun illumination.

¹Department of Physics and Astronomy and Wright Center for Photovoltaics Innovation and Commercialization, The University of Toledo, Toledo, OH, USA.

²Materials Science Center, National Renewable Energy Laboratory, Golden, CO, USA.

³Department of Chemistry and Biochemistry, The University of Toledo, Toledo, OH, USA.

^{*}e-mail: zhaoning.song@utoledo.edu; yanfa.yan@utoledo.edu

Organic-inorganic metal halide perovskite solar cells (PSCs) have reached a remarkable certified power conversion efficiency (PCE) of 25.2%¹. Perovskite/perovskite tandem solar cells are promising to further improve PCE and even break the Shockley-Queisser radiative limits for single-junction solar cells²⁻⁷. Recent advances in the low-bandgap mixed tin (Sn)lead (Pb) iodide PSCs have enabled the fabrication of efficient perovskite/perovskite tandem solar cells in both two-terminal (2-T) and four-terminal (4-T) configurations, with PCEs reaching more than 24% and 25%, respectively^{8, 9}. Despite the impressive progress⁷⁻¹⁸, the current state-of-the-art mixed Sn-Pb PSCs exhibit a significant shortcoming: they are either efficient stable, but not both. The high-efficiency **PSCs** or formamidinium/methylammonium (FA/MA)-based mixed Sn-Pb perovskite absorbers with a high MA proportion (≥30 mol%)^{11, 12, 19-22}. The high MA proportion leads to large perovskite grains that are critical for realizing high PCEs²³⁻²⁵. However, including a high proportion of volatile MA cations makes the devices unstable against heat and light stresses²⁶⁻²⁹. On the other hand, MA-free FA/cesium (Cs)-based mixed Sn-Pb perovskite absorbers exhibit high device stability under illumination. McGehee et al. recently demonstrated stable operation of PSCs based on FA_{0.75}Cs_{0.25}Sn_{0.4}Pb_{0.6}I₃ absorbers for up to 1000 hours¹⁴. For the FA/Cs-based mixed Sn-Pb PSCs, Cs was used to stabilize the perovskite phase, boosting the performance and stability⁷. However, the incorporation of a significant amount of Cs accelerates the perovskite crystallization process, leading to small grain sizes and a substantial number of grain boundaries, which compromise the PCE of resultant PSCs^{30, 31}. A viable way to overcome this dilemma is to synthesize high-quality FA-based mixed Sn-Pb perovskite films with large grains but low MA proportion. However, the current fabrication processes of mixed Sn-Pb PSCs are incapable of realizing the aforementioned goal. The most commonly used process to fabricate high PCE mixed Sn-Pb PSCs is based on the one-step process developed by Yan and coworkers.²⁰ Recently, Huang et al. incorporated a small dose of cadmium ions into FA_{0.5}MA_{0.45}Cs_{0.05}Pb_{0.5}Sn_{0.5}I₃ to enhance the electron diffusion length, achieving a PCE of about 20.0% for mixed Sn-Pb PSCs¹³. Tan and Sargent groups utilized a comproportionation process to suppress Sn²⁺ oxidation in mixed Sn-Pb perovskites. The PCE of single-junction FA_{0.7}MA_{0.3}Pb_{0.5}Sn_{0.5}I₃ PSCs has reached 21.1%, which enabled the fabrication of perovskite/perovskite tandem solar cells with a PCE of 24.8%. However, this one-step process has its limitation in preparing high-quality large-grained mixed Sn-Pb perovskite films when the MA proportion is below 30 mol%²⁰.

Here, we report a two-step bilayer interdiffusion growth (BIG) strategy to successfully reduce the MA proportion to 10% without compromising grain size and device performance. We further apply pyrrolidinium thiocyanate (PySCN) to form the one-dimensional (1D) PySn_xPb_{1-x}I₃ perovskite which passivates the film surface and grain boundaries^{32, 33}. As a result, the carrier lifetime of thick mixed Sn-Pb perovskite films is increased to 1.1 μs, which is essential for efficient photoexcited charge carrier collection in a thick absorber layer⁹. The incorporation of PySCN also improves the junction quality at the perovskite/electron transport layer (ETL) interface, boosting the open circuit voltage (V_{OC}) to 0.865 V. Our champion device based on the FA-based mixed Sn-Pb perovskite absorbers delivers a PCE of 20.4 (20.3)% measured under a reverse (forward) voltage scan, which is comparable with the best FA/MA-based mixed Sn-Pb PSCs^{8,9}. Benefiting from the reduced MA content and improved perovskite film quality, our mixed Sn-Pb PSCs show excellent stability against light and heat. An

encapsulated mixed Sn-Pb PSC retained 92% of its initial efficiency after 450 hours of continuous operation under one sun illumination.

Bilayer interdiffusion growth of FA-based mixed Sn-Pb perovskites

The two-step sequential deposition technique has been widely used for fabricating high-efficiency pure-Pb PSCs due to its simple and precise process control as well as good reproducibility³⁴. However, no success has been realized in mixed Sn-Pb perovskites with Sn ratio of ~50% due to the rapid crystallization of Sn-based perovskites³⁵. We first tested the synthesis of mixed Sn-Pb perovskite films via the conventional two-step method³⁴. Upon spin-coating the FAI/methylammonium chloride (MACl) in isopropyl alcohol (IPA) solution on a pre-deposited SnI₂/PbI₂ film, the film turned black rapidly, which is due to the stronger reaction of Sn²⁺ than Pb²⁺ with FAI³⁵. The rapid formation of small-sized perovskite grains blocks the diffusion of the organic halide salts, resulting in organic residues on the surface and unreacted SnI₂/PbI₂ at the bottom after annealing (**Supplementary Fig. 1**). The excess organic impurities cause excessive non-radiative recombination, while the unreacted SnI₂/PbI₂ hinders charge transport, limiting the device performance (**Supplementary Fig. 2**)³⁶.

To overcome the above issues, we designed the two-step BIG process with a prolonged ion diffusion and exchange stage to enable full conversion of SnI₂/PbI₂ into the perovskite phase, allowing for increased grain size of mixed Sn-Pb perovskites with a low MA concentration. **Fig. 1a** illustrates the process flow diagram of our BIG process. We employ additional MASCN (25 mol%) in the first-step SnI₂/PbI₂ precursor solution to promote the formation of mixed Sn-Pb perovskite nanocrystallites that help suppress the preferential rapid reaction between SnI₂ and FAI in the next step. MASCN is selected since SCN ions exhibit stronger bonding with Sn ions than halogen ions and can help suppress the oxidization of Sn²⁺³⁵. The SnI₂/PbI₂/MASCN precursor solution is first spin-coated on a substrate, and an FAI/IPA solution is subsequently spin-coated to form a bilayer precursor film. An interdiffusion stage at a low temperature of 50 °C is applied to promote the diffusion of FA ions and exchange of FA/MA cations, which allows the coalescence of the bilayer and completes conversion of precursors to the perovskite phase. This stage also enables a final annealing temperature of 120 °C, which provides sufficient thermal energy to promote grain growth and eliminate organic residues.

We tracked and analyzed the evolution of the crystal phase and microstructure of the mixed Sn-Pb perovskite films during the BIG process by X-ray diffraction (XRD) and scanning electron microscopy (SEM) measurements (**Fig. 1b-h**). The XRD pattern of a spin-coated SnI₂/PbI₂/MASCN precursor film shows a small peak at ~14.15° (**Fig. 1b**), corresponding to the (110) plane of MASn_{0.5}Pb_{0.5}I₃³⁷. The low peak intensity indicates that MASn_{0.5}Pb_{0.5}I₃ perovskite nanocrystallites have already formed in the as-prepared precursor film. The existence of solvents prevented their further growth. After a FAI/IPA solution was spin-coated onto the SnI₂/PbI₂/MASCN precursor film, the XRD peak of the (110) plane shifted to a lower angle of ~14° with slightly increased peak intensity (**Fig. 1b**), indicating that FA cations reacted with metal halides and started forming the FA-based perovskites. The top-view SEM image in **Fig. 1c** shows that small (300 – 500 nm in average size) but distinct grains were formed during this early stage, which correlates with the stronger XRD peak intensity. The corresponding cross-sectional SEM image (**Fig. 1f**) further reveals that the grains were formed in a bilayer

structure consisting of an upper layer of FA-based perovskite and a lower perovskite layer containing unreacted SnI₂/PbI₂/MASCN precursor complexes. A 50 °C annealing stage was then applied to promote FA diffusion and FA/MA ion exchange. The XRD pattern of a 50 °C annealed film (Fig. 1b) shows no obvious changes in the peak intensity or location, indicating the lack of sufficient thermal energy to promote grain growth. The top-view SEM image of this stage (Fig. 1d) shows the coalescence of grains, which results in a more uniform and smoother surface compared with the as-prepared film (Fig. 1c). The cross-sectional SEM (Fig. 1g) shows that the bilayer grains merged into a monolayer, which indicates the interdiffusion/ion exchange between the upper FA-based perovskite layer and the lower precursor complex layer²³. The final annealing at a relatively high temperature of 120 °C dramatically increased the diffraction peak intensity in the XRD pattern (Fig. 1b), indicating the enhanced grain size and crystallinity of the film. Additionally, the (110) peak shifted slightly toward a lower angle (13.98°), which is attributed to further MA/FA ion exchange promoted by higher thermal energy. No SnI₂/PbI₂ residual peak was detected by XRD, which confirms the complete conversion of SnI₂/PbI₂ into the perovskite phase. The high temperature annealing promoted grain growth to over 1 µm in average size (Fig. 1e), eliminating horizontal grain boundaries (Fig. 1h).

The diffusion stage at 50 °C is critical to synthesizing high-quality thick mixed Sn-Pb perovskite films. We first explored the annealing of the as-prepared film directly at 120 °C and found a layer of unreacted SnI₂/PbI₂ at the bottom of the perovskite layer (Supplementary Fig. 3). The metal iodide residues impede the extraction at the interface between the mixed Sn-Pb perovskite absorber layer and the poly(3,4-ethylenedioxythiophene):polystyrene sulfonate (PEDOT:PSS) hole-transport layer (HTL), limiting the performance of the resultant PSCs (Supplementary Fig. 4). The incomplete perovskite conversion is likely due to the fast evaporation of solvent at a high temperature which causes insufficient diffusion of FAI into the layer underneath. Thus, a diffusion stage at a mild temperature is needed to ensure sufficient ion exchange. However, the diffusion stage cannot be too long because a longer duration (e.g., 7 or 15 min) enlarges the grain size of the perovskite (Supplementary Fig. 5a-d) but severely deteriorates the crystallinity and grain integrity of the final perovskite films which show eroded and porous grains (Supplementary Fig. 5e-h). The XRD measurements (Supplementary Fig. 6) of the films with longer diffusion stage durations show lower peak intensities than that of the 3 min annealed film, corresponding to decreased crystallinity and undesirable film morphology.

The degradation caused by long-duration diffusion is attributed to the dynamic change of solvents in the film at this stage. We used temperature programmed desorption mass spectrometry (TPD-MS) to track the volatile species released from the 50 °C annealed perovskite film. We observed a high partial pressure of IPA at a relatively low temperature of ~50 °C and the release of DMF and DMSO at a higher temperature (~60 °C), along with the vaporization of excess FA in the form of its derivative fragments (**Supplementary Fig. 7**). Therefore, if the duration of pre-annealing at 50 °C exceeds its proper processing window, IPA will evaporate, and the remaining DMF/DMSO will re-dissolve and erode the perovskite during the diffusion stage. Also, the result shows that if the diffusion stage temperature exceeds 60 °C, faster evaporation of DMSO, DMF, and FA gases will lead to incomplete conversion as in the case of direct high temperature annealing (**Supplementary Fig. 6**). Therefore, optimal duration

(~3 min) and pre-annealing temperature (50 °C) are desired for the diffusion stage of the BIG process, which leads to high-quality mixed Sn-Pb perovskite films.

The thickness of mixed Sn-Pb perovskite films is determined by the concentration of the SnI_2/PbI_2 precursor solution. The perovskite film thickness increases from 600 ± 55 to $960 \pm$ 91 nm by changing the concentration of SnI₂/PbI₂/MASCN precursor solution from 1.4 to 1.7 M (Supplementary Figs. 8 and 9). For the mixed Sn-Pb perovskite, although a thicker absorber layer is preferred to ensure sufficient light absorption^{3, 13, 21}, the sub-bandgap defect state density increases with increasing the bulk volume of the film, as evident from the increasing Urbach energy measured by photothermal deflection spectroscopy (PDS, Supplementary Fig. 9). These sub-bandgap defect states cause charge recombination which shortens the carrier lifetime, lowering the V_{OC} and fill factor (FF) for the thicker mixed Sn-Pb PSCs (Supplementary Fig. 10). To balance the tradeoff between increasing photon absorption and avoiding defect formation, an optimal thickness of 900 \pm 69 nm by using the 1.6 M precursor solution is selected. The mixed Sn-Pb perovskite film prepared by the BIG method shows a carrier lifetime of 565 ns and a Urbach energy of 26.7 ± 1 meV, which are comparable to those of the single-step processed (FASnI₃)_{0.6}(MAPbI₃)_{0.4} perovskite films (Supplementary Fig. 11). The long carrier lifetime and low defect density are desired for high-performance PSCs⁹.

To evaluate the photovoltaic (PV) performance of the mixed Sn-Pb perovskite films prepared by the BIG process, we utilized this method to fabricate PSCs with a p-i-n configuration of glass/indium tin oxide (ITO)/PEDOT:PSS/perovskite/fullerene (C_{60}) /bathocuproine (BCP)/Ag. It is known that the addition of alkali cations such as Cs^+ and Rb⁺ are beneficial to the device performance because they can increase entropy, modify the tolerance factor, and reduce lattice strains^{16, 38-41}. Here, 5 mol% CsI was incorporated to improve reproducibility and eliminate the hysteresis in current-voltage (J-V) measurements (Supplementary Fig. 12) of the mixed Sn-Pb PSCs without changing the chemical phase and microstructure of the perovskite thin films (Supplementary Fig. 13). The bandgap of the Cscontaining mixed Sn-Pb film measured by spectroscopic ellipsometry is 1.28 eV (Supplementary Fig. 14), which is consistent with the other mixed Sn-Pb perovskites with a Sn/Pb atomic ratio of 1:1 reported in the literature^{42, 43}. We fabricated 30 PSCs using the BIG processed mixed Sn-Pb perovskite absorber layers, and the statistics of the PV parameters are summarized in Supplementary Table 1 and Supplementary Fig. 15. The average PCEs of the 5 mol% CsI containing PSCs are 18.91 ± 0.36 (18.86 ± 0.35) % under reverse (forward) voltage scan, showing negligible J-V hysteresis (Supplementary Fig. 12).

Impact of MA concentration on film thermal stability

Proton nuclear magnetic resonance (¹H NMR) was used to quantitatively analyze the molar ratio of FA/MA in the BIG processed mixed Sn-Pb perovskite films. We made several perovskite films using the BIG process and scraped the perovskite powders from the substrates. The perovskite powders were then dissolved in DMSO-d₆ for the ¹H NMR measurement, and the spectrum is shown in **Supplementary Fig. 16.** The histogram analysis of the normalized NMR peaks intensity corresponding to individual chemical species is shown in **Fig. 2a**, from

which the composition of our BIG processed mixed Sn-Pb perovskite is estimated to be about $FA_{0.85}MA_{0.1}Cs_{0.05}Sn_{0.5}Pb_{0.5}I_3$.

We then performed TPD-MS measurements to compare the thermal stability of a BIG-processed FA_{0.85}MA_{0.1}Cs_{0.05}Sn_{0.5}Pb_{0.5}I₃ perovskite film with a (FASnI₃)_{0.6}(MAPbI₃)_{0.4} film prepared by the one-step method. The (FASnI₃)_{0.6}(MAPbI₃)_{0.4} film released MA (CH₃NH₂) and hydroiodic acid (HI) gas species at a low temperature of ~68 °C and became more pronounced with increasing temperature, indicating the commencement of thermal decomposition at ~68 °C (**Fig. 2b**). In contrast, the FA_{0.85}MA_{0.1}Cs_{0.05}Sn_{0.5}Pb_{0.5}I₃ film prepared by the BIG method shows much improved thermal stability with MA and FA fragments releasing at ~125 °C (**Fig. 2c** and **Supplementary Fig. 17**). Interestingly, the release of HI signal starts later than that of the organic species at ~170 °C which indicates the lower MA content makes the mixed Sn-Pb perovskite more thermally stable. We then performed a more thorough thermal stability study of various mixed Sn-Pb films and confirmed that reducing the MA content is indeed beneficial for the stability of mixed Sn-Pb perovskite films (**Supplementary Fig. 18** and **Supplementary Fig. 19**).

Time of flight secondary ion mass spectroscopy (ToF-SIMS) measurement was performed to probe the depth profile of a FA_{0.85}MA_{0.1}Cs_{0.05}Sn_{0.5}Pb_{0.5}I₃ perovskite film. As shown in Fig. 2d, the signals corresponding to Sn²⁺, Pb²⁺, I⁻, and FA⁺ are almost constant throughout the film thickness, which indicates the uniform distribution of these elements. Interestingly, the MA⁺ signal shows a decreasing gradient from the film surface (0 nm) to the perovskite/ITO glass interface, whereas the signal of Cs⁺ shows a positive gradient. Although the unusual increased signal intensity in the surface region (~50 nm) could be due to the degradation during sample shipment or ion beam damage⁴⁴, the trends of MA⁺ and Cs⁺ are complementary in the bulk of the perovskite. The higher concentration of Cs⁺ at the bottom may be due to the lower diffusion coefficient of Cs⁺ than that of MA⁺. The component distribution indicates the MA concentration is relatively higher in the surface region than in the film bulk region, as illustrated in Fig. 2e. The MA ions in the surface are easier to decompose by heat and light stresses, which is in good agreement with the short release period of MA species in Fig. 2c and Supplementary Fig. 20. The formed MA and I vacancies will lead to the formation of recombination centers which degrades PSCs performance⁴⁵⁻⁴⁷. Therefore, a strategy to passivate the top surface of BIG-processed mixed Sn-Pb perovskite films is needed.

Surface passivation using 1D pyrrolidine perovskite

We introduced the 1D PySn_xPb_{1-x}I₃ perovskite to passivate the surface and grain boundaries of our BIG processed FA_{0.85}MA_{0.1}Cs_{0.05}Sn_{0.5}Pb_{0.5}I₃ perovskite films. The impact of PySCN proportion on the chemical phase and microstructure of mixed Sn-Pb perovskites was studied (Supplementary Fig. 21 and Supplementary Fig. 22)³². When the PySCN proportion is increased to 5 mol%, the grain size is reduced, and pinholes and voids between grains are formed (Supplementary Fig. 22d). The voids will cause undesirable recombination which adversely affects device performance. Incorporation of an optimal proportion (1.5 mol%) of PySCN enhances the PL emission and increases the mean carrier lifetime from 670 ns to 1.1 µs (Fig. 3a and Supplementary Fig. 23). The microsecond lifetime is comparable with the lifetime of high-quality FA/MA-based mixed Sn-Pb perovskites⁹. The prolonged carrier

lifetime is attributed to the grain boundary passivation by 1D-PySn_xPb_{1-x}I₃ perovskites. The surface potential mapping shows a more pronounced upward potential bending at grain boundaries of the mixed Sn-Pb film after the addition of PySCN (**Supplementary Fig. 24**), indicating stronger electron attraction and hole repulsion at grain boundaries, which is known as a feature of defect passivation⁵⁰.

The formation of 1D PySn_xPb_{1-x}I₃ perovskites on the surface of mixed Sn-Pb perovskite absorber layers also favorably influence junction quality, as revealed by cross-sectional Kelvin probe force microscopy (KPFM) measurements. The potential line profiles, potential differences with respect to the zero bias, and electrical field difference are shown in **Supplementary Fig. 25** and **Fig. 3b and c**. Without the PySCN incorporation, a small peak is seen at the HTL/perovskite junction in the electrical field difference profiles measured with various bias, beside the main peak at the perovskite/ETL junction (**Fig. 3b**). However, with 1.5 mol% PySCN incorporation, the peak at the HTL/perovskite junction disappeared, leaving only the peak at the perovskite/ETL junction (**Fig. 3c**). This behavior is clear evidence of improved junctions, as we demonstrated previously in various perovskite device configurations⁴⁸⁻⁵⁰. This positive effect on junction quality and enhanced carrier lifetime led to improved V_{OC} and FF when a small amount of PySCN is incorporated. The V_{OC} reaches a maximum when the incorporation of PySCN reaches 1.5 mol% (**Supplementary Fig. 26**).

High performance and stability single-junction and tandem PSCs

We fabricated single-junction mixed Sn-Pb PSCs using the 1.5 mol% PySCN incorporated FA_{0.85}MA_{0.1}Cs_{0.05}Sn_{0.5}Pb_{0.5}I₃ perovskites as the absorber layers. Fig 4a shows the histogram of PCEs of 30 cells. The detailed PV parameters of the PCSs are shown in Supplementary Fig. 27 and Supplementary Table 2, showing good reproducibility and negligible J-V hysteresis. The noticeable improvements in V_{OC} and FF due to the PySn_xPb_{1-x}I₃ passivation are observed. Fig. 4b shows the J-V curves of the best-performing device measured under reverse and forward voltage scans. The cell delivers a PCE of 20.4 (20.3)%, a V_{OC} of 0.865 (0.864) V, a J_{SC} of 29.81 (29.85) mA/cm², and a FF of 79.1 (78.7)% under the reverse (forward) voltage scan. The J_{SC} values match well with the integrated photocurrent density of 29.33 mA/cm² deduced from the external quantum efficiency (EQE) spectrum (Fig. 4c). More importantly, the FA-based mixed Sn-Pb PSCs show decent operational stability. As shown in Fig. 4g, an encapsulated FA_{0.85}MA_{0.1}Cs_{0.05}Sn_{0.5}Pb_{0.5}I₃ cell retained 92 % of its original efficiency after maximum power point (MPP) tracking for 450 hours under continuous 1 Sun illumination. This robust operational stability is mainly attributed to the BIG-processed FA-based mixed Sn-Pb perovskite after comparing devices with different compositions and passivation (Supplementary Fig. 28 and Supplementary Fig. 29). Moreover, we performed an accelerated thermal degradation test of mixed Sn-Pb PSCs following the perovskite community consensus 51 . We found that the BIG processed $FA_{0.85}MA_{0.1}Cs_{0.05}Sn_{0.5}Pb_{0.5}I_3$ PSCs demonstrated considerably improved intrinsic thermal stability compared with the conventional (FASnI₃)_{0.6}(MAPbI₃)_{0.4} when aged at 85 °C in nitrogen. (Supplementary Fig. 30). It has been found that the thermal stability of most mixed Sn-Pb PSCs is limited by the use of acidic PEDOT:PSS and corrosive Ag electrode¹⁴. The real-world applications of mixed Sn-Pb PSCs require more stable HTLs, electrodes, and encapsulation techniques.

The stable low-bandgap FA-based mixed Sn-Pb PSCs enabled us to fabricate stable 2-T perovskite/perovskite tandem solar cells. The tandem cells consisting of 1.73 eV wide-bandgap top subcells and the 1.28 eV BIG-processed low-bandgap bottom subcells were fabricated following the procedure reported previously¹². The device architecture is depicted in Supplementary Fig. 31, and the corresponding cross-sectional SEM image is shown in Fig. 4d. Benefiting from the high-quality mixed Sn-Pb subcell prepared by the BIG process with the PySn_xPb_{1-x}I₃ passivation, the champion tandem cell exhibited a PCE of 23.3 (23.3)%, with a high V_{OC} of 1.943 (1.937) V, J_{SC} of 15.1 (15.2) mA/cm², and a FF of 79.3 (79) % under the reverse (forward) voltage scan (Fig. 4e). The integrated J_{SC} values for wide- and low-bandgap subcells calculated from the EQE spectra (Fig. 4f) are 15.0 and 14.8 mA/cm², respectively, which are consistent with the J_{SC} value from the J-V curves. The stable low-bandgap mixed Sn-Pb subcells enable the stable operation of our perovskite/perovskite tandem solar cells. Fig. 4g illustrates that an encapsulated 2-T perovskite/perovskite tandem solar cell retained 85 % of its initial PCE after MMP tracking for more than 350 hours under 1 sun illumination, which is significantly improved compared with the device using the conventional mixed Sn-Pb subcell (Supplementary Fig. 32).

Conclusion

In summary, we developed a two-step BIG process to fabricate high-efficiency and highstability FA-based mixed Sn-Pb PSCs. The deposition process was systematically investigated to understand the perovskite formation mechanism. The mixed Sn-Pb absorber films exhibited low MA concentration. Single-junction **PSCs** a FA_{0.85}MA_{0.1}Cs_{0.05}Sn_{0.5}Pb_{0.5}I₃ absorber layers prepared by the BIG process achieved a best PCE of 20.4 % and demonstrated MPP stability for more than 450 hours of continuous operation with a power loss of less than 10%. The stable low-bandgap mixed Sn-Pb PSCs enabled the fabrication of 2-T perovskite/perovskite tandem cells with PCEs exceeding 23%. A tandem cell retained 85 % of its initial PCE after 350 hours of continuous operation under MPP tracking. Our BIG process paves a pathway to simultaneously fabricate high-performance and highstability mixed Sn-Pb PSCs. However, further improvements in design of the device architecture and selection of materials are needed to enable better PCE and stability of tandem cells.

Figures

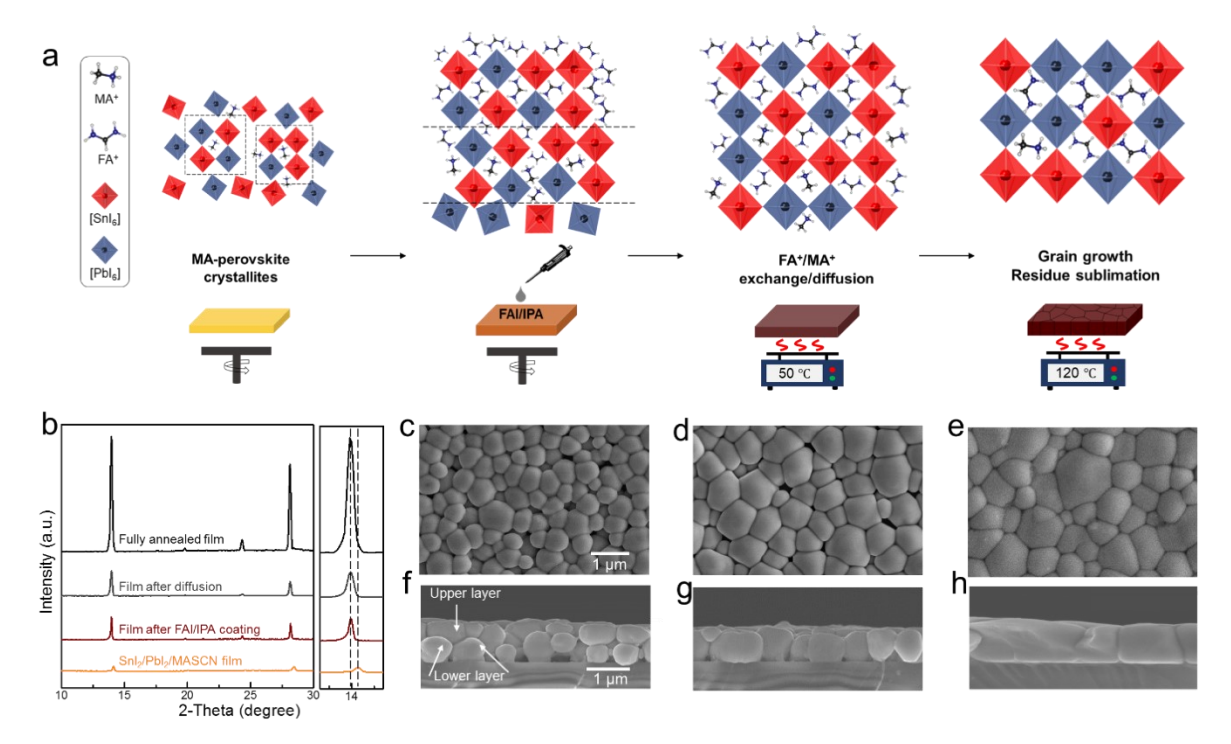


Fig. 1 Mixed Sn-Pb perovskite films prepared by the BIG process. a, Schematic diagram of the BIG process. **b**, XRD patterns of films at each processing stage. **c** (**f**), **d** (**g**), and **e** (**h**), top-view (cross-sectoinal) SEM images of the perovskite films after FAI/IPA coating, the diffusion stage, and final annealing, respectively.

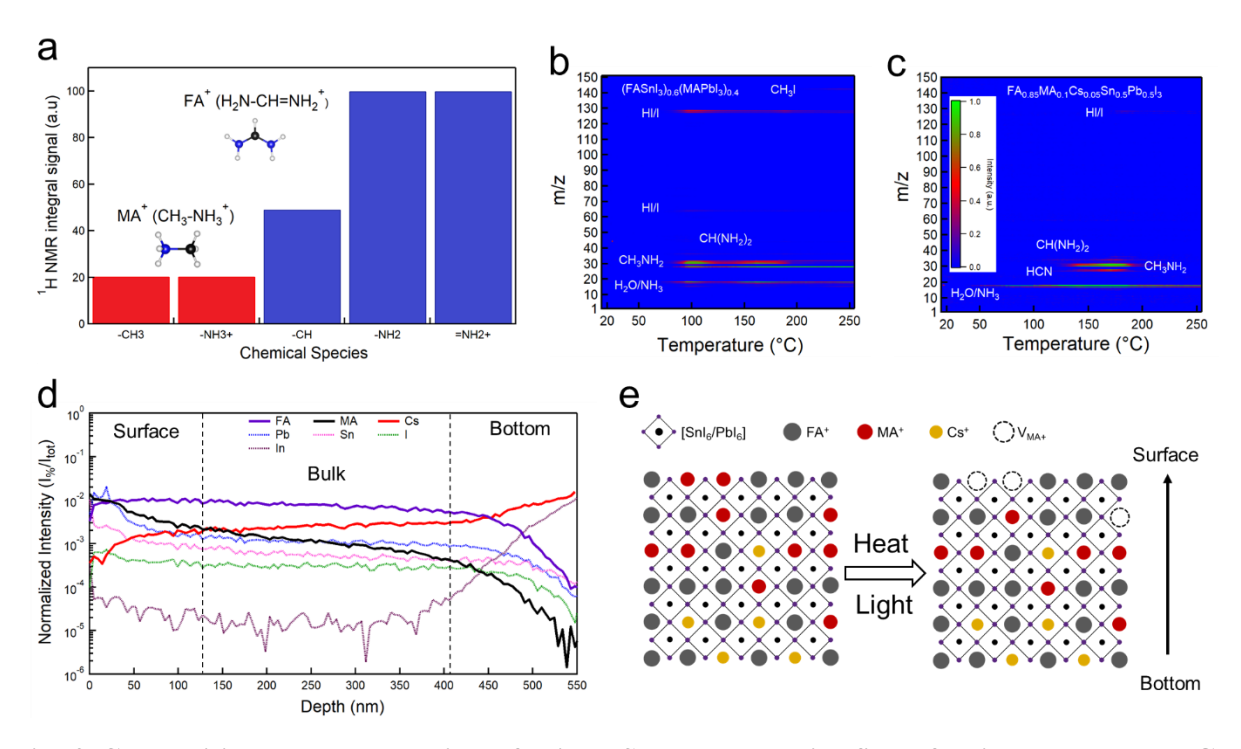


Fig. 2 Composition and degradation of mixed Sn-Pb perovskite films fabricated by the BIG process. a, 1H NMR analysis of mixed Sn-Pb perovskites prepared by the BIG process. b and c, TPD-MS of $(FASnI_3)_{0.6}(MAPbI_3)_{0.4}$ and $FA_{0.85}MA_{0.1}Cs_{0.05}Sn_{0.5}Pb_{0.5}I_3$ perovskite films. d, ToF-SIMS of $FA_{0.85}MA_{0.1}Cs_{0.05}Sn_{0.5}Pb_{0.5}I_3$ perovskite film made by the BIG process. e, Schematic diagram of elemental distribution in the $FA_{0.85}MA_{0.1}Cs_{0.05}Sn_{0.5}Pb_{0.5}I_3$ film and surface degradation due to heat and light stresses.

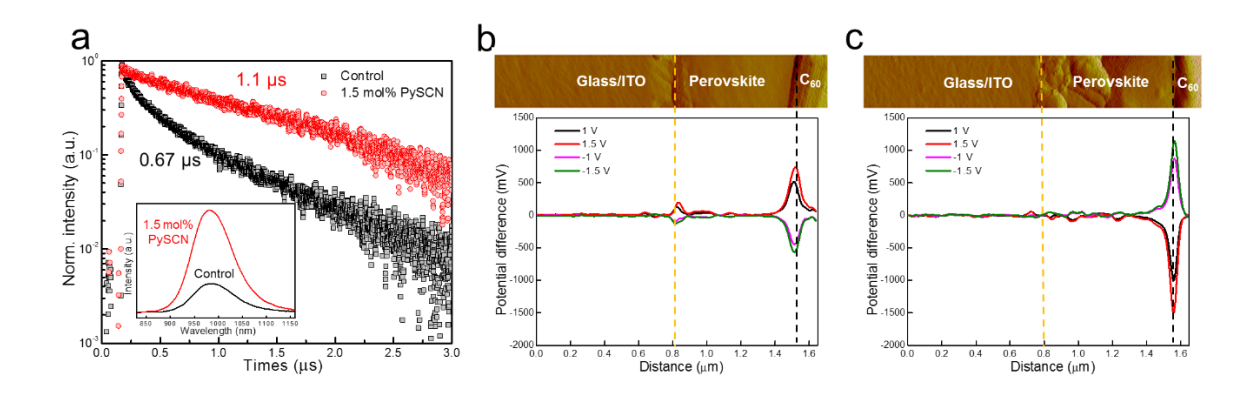


Fig. 3 1D PySn_xPb_{1-x}I₃ passivation of mixed Sn-Pb perovskite thin films. a, TRPL decays and PL spectra (inset) of the FA_{0.85}MA_{0.1}Cs_{0.05}Sn_{0.5}Pb_{0.5}I₃ perovskite films without (control) and with 1.5 mol% PySCN. b and c, cross-sectional KPFM potential maps and the corresponding electric field profiles of the FA_{0.85}MA_{0.1}Cs_{0.05}Sn_{0.5}Pb_{0.5}I₃ films without and with 1.5 mol% PySCN.

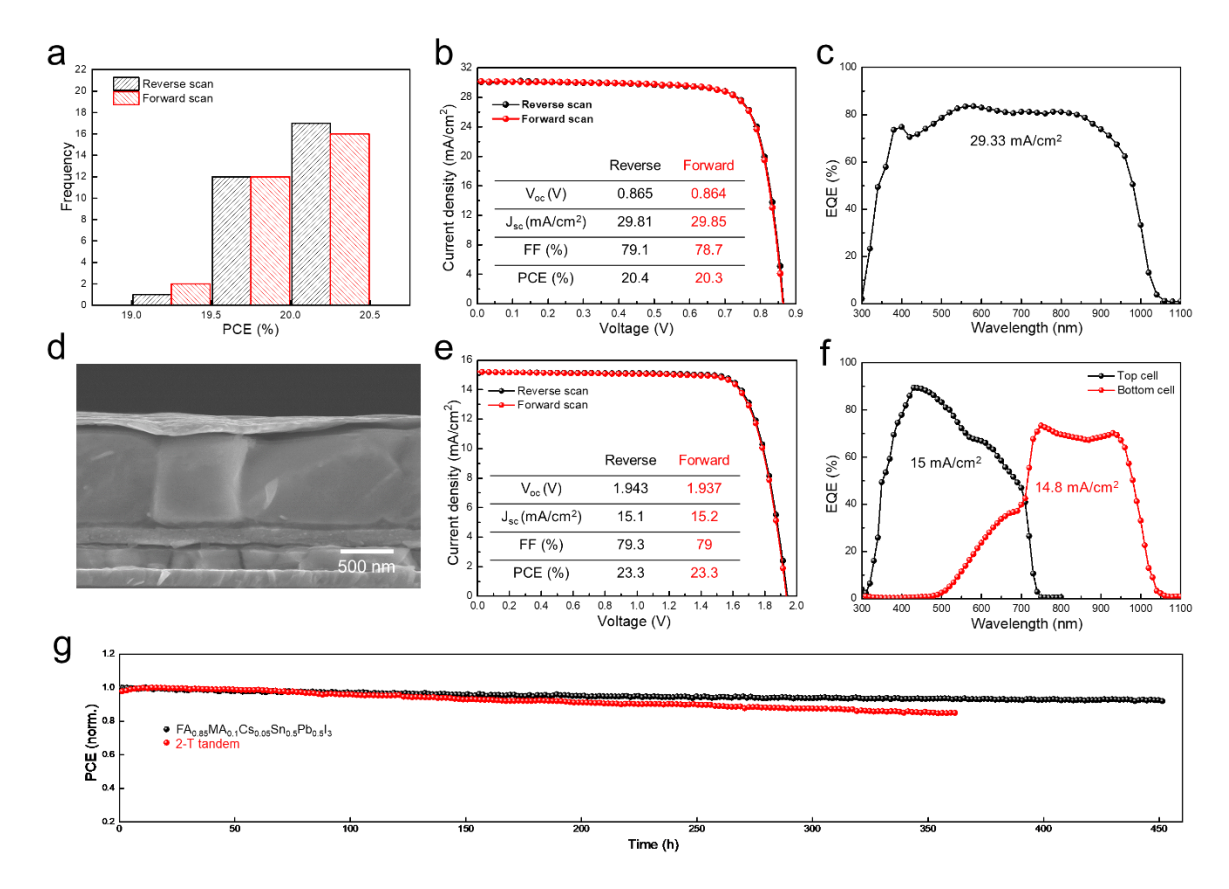


Fig. 4 Single-junction and tandem PSCs. a, Histogram of the PCEs for 30 FA_{0.85}MA_{0.1}Cs_{0.05}Sn_{0.5}Pb_{0.5}I₃ mixed Sn-Pb PSCs with 1.5 mol% PySCN. b and c, J-V curves and EQE spectrum of the best-performing single-junction mixed Sn-Pb PSC. d, Cross-sectional SEM image of a perovskite/perovskite tandem solar cell. e and f, J-V curves and EQE spectrum of the best-performing perovskite/perovskite tandem solar cell. g, MPP tracking of a FA_{0.85}MA_{0.1}Cs_{0.05}Sn_{0.5}Pb_{0.5}I₃ PSC and a 2-T perovskite/perovskite tandem cell with encapsulation measured in the air under simulated AM1.5G solar illumination.

Methods

Materials. Tin(II) iodide (SnI₂), lead thiocyanate (Pb(SCN)₂), methylammonium chloride (MACl), diethyl ether, tin(II) fluoride (SnF₂), N,N-dimethylmethanamide (DMF), dimethyl sulfoxide (DMSO) and isopropanol (IPA) were purchased from Aldrich Sigma. Lead iodide (PbI₂) and cesium iodide (CsI) were purchased from Alfa Aesar. Formamidinium iodide (FAI), methylammonium iodide (MAI), methylammonium thiocyanate (MASCN) and pyrrolidinium thiocyanate (PySCN) were purchased from GreatCell Solar. Poly(triaryl amine) (PTAA) was purchased from Xi'an Polymer Light Technology Corp. Poly(3,4-ethylenedioxythiophene):polystyrene sulfonate (PEDOT:PSS) was purchased from Heraeus company. 2,3,5,6-Tetrafuoro-7,7,8,8-tetracyanoquinodimethane (F4TCNQ) and bathocuproine (BCP) were purchased from Jilin OLED Company. Indium tin oxide (ITO) target and silver were purchased from Kurt J. Lesker.

One-step (FASnI₃)_{0.6}(MAPbI₃)_{0.4} low-bandgap perovskite precursor. The precursor solution was prepared by the same recipe reported in our previous work. 372 mg SnI₂, 172 mg FAI and 15.6 mg SnF₂ were dissolved in 424 μL DMF and 212 μL DMSO mixed solvent to prepare FASnI₃ precursor solution. 461 mg PbI₂, 159 mg MAI, and 11.3 mg Pb(SCN)₂ were dissolved in 633 μL DMF and 71 μL DMSO mixed solvent. The two solutions were then mixed at the molar ratio of 6:4 to form the (FASnI₃)_{0.6}(MAPbI₃)_{0.4} precursor solution.

Two-step conventional mixed Sn-Pb low-bandgap perovskite precursor. 345.8 mg PbI_2 and 279.5 mg SnI_2 were dissolved in 900 μ L DMF and 100 μ L DMSO mixed solvent to form the first step precursor solution. 60 mg FAI and 6 mg MACl were dissolved in 1 μ L IPA to form the second step precursor.

Two-step BIG processed FA_{0.85}MA_{0.1}Cs_{0.05}Sn_{0.5}Pb_{0.5}I₃ perovskite precursor. 230.5 mg PbI₂, 186.3 mg SnI₂, 12.99 mg CsI, and 22.54 mg MASCN were dissolved in DMF and DMSO mixed solvent for the FA_{0.85}MA_{0.1}Cs_{0.05}Sn_{0.5}Pb_{0.5}I₃ precursor. CsI was removed from the recipe to prepare the FA-based mixed Sn-Pb perovskite without Cs⁺, while everything else remains the same. To change the precursor solution concentration, the mixed DMF/DMSO solvent of 714/51, 667/47, 625/44 and 588/42 μL were used to prepare the 1.4, 1.5, 1.6 and 1.7 *M* precursor solution respectively. Additional 1.3, 2.0, and 6.5 mg PySCN were added to the precursor to form 1, 1.5 and 5 mol% PySn_xPb_{1-x}I₃ passivation. 60 mg FAI were dissolved in 1 μL IPA to form the second step precursor.

FA_{0.8}Cs_{0.2}Pb(I_{0.7}Br_{0.3})₃ wide-bandgap perovskite precursor. 126.6 mg FAI, 47.8 mg CsI, 152.0 mg PbBr₂, and 233.2 mg PbI₂ were dissolved in the mixed solvent of 750 μL DMF and 250 μL DMSO.

One-step (FASnI₃)_{0.6}(MAPbI₃)_{0.4} low-bandgap PSCs fabrication. The hole transport layer (HTL) PEDOT:PSS was spin-coated on ITO substrate at 4,000 r.p.m. for 50s, followed by a 150 °C annealing for 15 minutes. 40 μL of the perovskite solution was spin-coated on the PEDOT:PSS layer at 5,000 r.p.m. for 60 s. Diethyl ether was applied dropwise onto the film at 5s from the start of the spin. The film was then transferred to a 100 °C hotplate for 7 minutes. After cooling to the room temperature, the film was kept in a sealed box and then transferred to Kurt J. Lesker thermal evaporation system. 20 nm C₆₀, 5 nm BCP and 80 nm Ag were sequentially evaporated on the perovskite film to form a PSC device. Unless otherwise mentioned, the HTL, ETL, and electrode fabrication process were the same for other low-bandgap PSCs.

Two-step conventional mixed Sn-Pb low-bandgap PSC fabrication. 40 μ L SnI₂/PbI₂ precursor solution was spin-coated on PEDOT:PSS at 1,500 r.p.m. for 30s, followed by a 70 °C annealing for 2 minutes. After spin, 150 μ L FAI/MACl solution was dropped on the precursor film and the excess solution was spin-dry immediately by another 1,500 r.p.m. spin for 30s. The film was then annealed on a 100 °C hotplate before transferred to the evaporation system to fabricated ETL and electrode.

Two-step BIG processed FA_{0.85}MA_{0.1}Cs_{0.05}Sn_{0.5}Pb_{0.5}I₃ PSC fabrication. 40 μL of the first step precursor solution SnI₂/PbI₂/MASCN/CsI/PySCN was spin-coated on PEDOT:PSS substrate at 1,500 r.p.m. for 30s. Then 200 μL of the second step FAI precursor solution was dropped on the precursor film followed by an immediately spin of 1,500 r.p.m for another 30 s. The delay between applying FAI and second step spinning was required to be finished within 1s. The film was then transferred to a 50 °C hotplate for 3 minutes for the diffusion of FAI and fully transformation of perovskite phase. Afterwards, the film was transferred to a 120 °C hotplate for 7 minutes for further grain growth. The annealed film was then sealed and transferred to the evaporation system to fabricated ETL and electrode.

2-T perovskite/perovskite tandem solar cell fabrication. 80 μL PTAA solution was spin-coated on the ITO substrate at 4000 r.p.m. for 30 s and then the substrate was annealed at 100 °C for 10 minutes. 70 μL DMF was spin-coated at 4000 r.p.m. for 10 s to improve the wettability of PTAA surface prior to wide-bandgap perovskite deposition. The perovskite precursor was spin-coated at 500 r.p.m. for 3s and then 4000 r.p.m. for 60 s. During the 4000 r.p.m. step, 750 μL diethyl ether was applied dropwise in the center of the substrate to facilitate the crystallization. After that, the substrate was annealed at 60 °C for 2 minutes and 100 °C for 5 minutes. Next, the substrate was transferred to the vacuum chamber. 20 nm C₆₀ and 5 nm BCP were thermally evaporated sequentially. The substrate was then transferred to the radio frequency magnetron sputtering system. 130 nm ITO layer was sputtered from the 3 inche ITO target (Lesker, In₂O₃/SnO₂ 90/10 wt%) at a 70 W power under Ar pressure of 2 mtorr. Then diluted PEDOT:PSS with IPA (volume ratio 1:1) was spin-coated on the sputtering ITO layer, followed by a 5 minutes annealing at 100 °C hotplate in the air. After annealing, the film was transferred to glove box immediately for the BIG processed FA_{0.85}MA_{0.1}Cs_{0.05}Sn_{0.5}Pb_{0.5}I₃ layer deposition, which followed the same process as discussed above. Finally, the film was transferred in a sealed box to the thermal evaporation system to evaporate ETL and electrode.

XRD. Rigaku Ultima III XRD with Cu K_{α} radiation was used to measure and analyze the crystal structure and properties of the one step processed, conventional processed low-bandgap mixed Sn-Pb perovskites, and the $FA_{0.85}MA_{0.1}Cs_{0.05}Sn_{0.5}Pb_{0.5}I_3$ precursor films at each stage during the BIG process as well as the films with different concentration of PySCN passivation.

SEM. High-resolution field-emission Hitachi S-4800 SEM was used to measure the top view and cross-sectional images of the conventional processed low-bandgap mixed Sn-Pb perovskites, and the $FA_{0.85}MA_{0.1}Cs_{0.05}Sn_{0.5}Pb_{0.5}I_3$ precursor films at each stage during the BIG process, as well as the films with different concentration of PySCN passivation.

KPFM. Scanning Kelvin probe force microscopy measurements were performed in an Ar-filled glovebox using a Vecco D5000 atomic force microscope. A PPP-EFM tip operates in tapping mode for the cross-sectional potential distribution. The electrical resolution is ~10 mV. In the junction measurement, we cleaved the solar cell to expose the cross-sectional surface; the ITO was grounded and various of bias voltages were applied to the Ag side. No polishing or ion-milling treatment were introduced to the sample preparation to avoid artifacts.

Photothermal deflection spectroscopy (PDS) measurement. PDS measurements were collected using a custom system (PTS-3-PTD, Sciencetech Inc.) operating in transverse configuration⁵² over a spectral range of 1400 - 800 nm (0.89 - 1.55 eV) in 10 nm steps. The monochromatic pump beam was modulated with a mechanical chopper at 0.2 Hz. The probe beam was a 633 nm laser of nominally 300 μ m cross sectional diameter. Perovskite films were placed into a quartz cuvette which was then filled with FluorinertTM (C_6F_{14} fluid) while inside a nitrogen purged glove box. PDS measurements were collected for perovskite films without exposure to atmosphere.

¹H NMR. The Proton spectrum were acquired on a Bruker Avance III NMR spectrometer with a DCH Cryoprobe at 600 MHz. The data was collected at 22 °C using a 1-pulse sequence with a 30 degrees flip pulse of 3.3 microseconds, acquisition time of 2.7 seconds and a recycle delay of 1 second.

TPD-MS. The TPD-MS measurements were performed using a built-in-house TPD system. The mass spectra in a range of 1 to 150 atomic mass units (AMU) were recorded by a quadrupole mass spectrometer (Stanford Research System, RGA 300) using a custom LabVIEW program, following the previously reported procedure. For a typical TPD routine, the furnace temperature was ramped up from room temperature to 500 °C at a ramp rate of 1.67 °C/min.

ToF-SIMS. An ION-TOF TOF-SIMS V Time of Flight SIMS (TOF-SIMS) spectrometer was used for depth profiling and chemical imaging of the perovskite. Analysis was completed using a 3-lens 30-kV BiMn primary-ion gun. 1D profiles were completed utilizing the Bi3+ primary-ion beam, (0.8-pA pulsed beam current), and a 50×50-μm area was analyzed with a 128:128 primary beam raster. Sputtering for surface cleaning and depth profiling was accomplished with 1-kV oxygen and cesium ion sputter beams (~5-nA sputter current for each source) with a raster of 200×200 μm. After completion of the SIMS measurements, the depth of the SIMS sputter craters was determined by optical interference light microscopy to convert the SIMS sputter time scale to a sputter depth scale.

TRPL. TRPL measurements were conducted using a time correlated single photon counting (TCSPC) module (Becker & Hickel Simple Tau SPCM 130-E/M module). Samples were excited by a 532 nm pulsed laser (Fianium model SC400-2, ~5 ps pulse width, ~150 μm spot diameter) at ~10¹⁰ photons pulse⁻¹ cm⁻². Radiative recombination events were detected via an InP/InGaAsP NIR PMT detector (Hamamatsu H10330A-45) after dispersion by an iHR-320 monochromator (900 g/mm, 850 nm blaze) grating. PL decay curves were biexponential in nature and fitted by iterative re-convolution with the measured system response function. Mean photogenerated carrier lifetime for the biexponential fit is calculated by the weighted average method.

Spectroscopic ellipsometry (SE) and unpolarized transmittance measurement. Immediately following PDS measurement, each film was removed from the C_6F_{14} fluid into the laboratory ambient for SE and unpolarized transmittance measurements. Both measurements were collected using a multichannel rotating-compensator spectroscopic ellipsometer (M-2000FI, J. A. Woollam Co., Inc.) over a spectral range of 1676 - 210 nm (0.74 - 5.89 eV). The SE and unpolarized transmittance measurements were collected at 70° and 0° angle of incidence, respectively, with the SE being measured in terms of $N = \cos(2\psi)$, $C = \sin(2\psi)\cos\Delta$, and $S = \sin(2\psi)\sin\Delta$. The combined time for sample mounting, alignment, and data acquisition for these two measurements, i.e. the length of time the films were in laboratory ambient air, was approximately 2 to 3 mins.

PSC Characterization. The PSCs were encapsulated with cover glasses and then sealed by ultraviolet-curable epoxy before conducting the J-V measurement, MMP tracking measurement and EQE measurement in ambient. J-V curves were measured under 100 mW cm⁻² AM1.5G solar irradiation (PV Measurements Inc.) with a Keithley 2400 Source Meter.

The light intensity for *J–V* measurements was calibrated by a standard silicon wafer solar cell and the perovskite solar cells certified by Newport. The MMP tracking measurement for both FA_{0.85}MA_{0.1}Cs_{0.05}Sn_{0.5}Pb_{0.5}I₃ single-junction PSC and the fabricated 2-T tandem cell were conducted in the air under a full spectrum one sun illumination without any light filter. The humidity of the measurement environment ranged from 40% to 60%. Especially, the single-junction FA_{0.85}MA_{0.1}Cs_{0.05}Sn_{0.5}Pb_{0.5}I₃ PSC was tracked under room temperature while for the 2-T tandem cells the environment temperature was kept at 25 °C to limit the water and oxygen ingression through the encapsulant from the humid measurement environment. A 0.1 cm² area mask was used to define the active area of a PSC. A QE system (PV Measurements Inc., model IVQE8-C) was used to measure the

quantum efficiency of the PSCs. A standard silicon wafer solar cell was used as the reference for the EQE measurement. We used bias illumination to measure the EQE for 2-T tandem cell. The EQE of top and bottom sub-cells were measured by exposing the 2-T tandem cell under a 530 nm and 940 nm LED lamp respectively to saturate the other junction during EQE measurement. The thermal stability tests were conducted by aging the PEDOT:PSS-free devices on a hotplate at 85 °C in a nitrogen glovebox. The devices were then encapsulated and periodically took out to the ambient air for J-V measurements. Once the measurement of a device was done, the device was placed back to the hotplate in the glovebox immediately to prevent inevitable leakage and oxidization.

Acknowledgments

This material is based upon work supported by the U.S. Department of Energy's Office of Energy Efficiency and Renewable Energy (EERE) under the Solar Energy Technologies Office Award Number DE-EE0008753. The TPD-MS study is supported by National Science Foundation under contract number DMR-1807818. K.S. and R.E. were supported by the U.S. Air Force Research Laboratory under agreement number FA9453-18-2-0037, and N.S., B. S., N. P., and R.E. were supported by the U.S. Air Force Research Laboratory under agreement number FA9453-19-C-1002. The U.S. Government is authorized to reproduce and distribute reprints for Governmental purposes notwithstanding any copyright notation thereon.

Competing interests

The authors declare no competing financial interests.

Author contribution

C.L., Z.S. and Y.Y. conceived the project. C.L. carried out the single-junction low-bandgap cell and tandem cell fabrication. C.C. prepared the wide-bandgap cell and helped the tandem cell fabrication. D.L. participated in the wide bandgap cell fabrication. Z.S. conducted the TPD-MS measurement. C.X. and C.J. helped with KPFM. B.S. conducted the PDS and spectroscopic ellipsometry measurement. S.H. conducted the ToF-SIMS measurement. N.S. and K.K.S. helped with PL and TRPL measurement. L.C. and Y.L. participated in the characterization. Y.W.K. helped the ¹H NMR measurement. C.L., Z.S., and Y.Y. analyzed the data and wrote the manuscript. M.H., D.Z., R.E., N.P. and M.A.J. helped with the manuscript preparation. All the authors discussed the results and commented on the manuscript. Y.Y. supervised the project.

- 1. *Best research-cell efciencies* (nrel, 2020); https://www.Nrel.Gov/pv/assets/pdfs/best-research-cell-efficiencies.20200311.Pdf.
- 2. Shockley, W., Queisser, H. J. Detailed balance limit of efficiency of p-n junction solar cells. *Journal of Applied Physics* **32**, 510-519 (1961).
- 3. Hörantner, M. T., *et al.* The potential of multijunction perovskite solar cells. *ACS Energy Letters* **2**, 2506-2513 (2017).
- 4. Leijtens, T., Bush, K. A., Prasanna, R., McGehee, M. D. Opportunities and challenges for tandem solar cells using metal halide perovskite semiconductors. *Nature Energy* **3**, 828-838 (2018).

- 5. Lal, N. N., Dkhissi, Y., Li, W., Hou, Q., Cheng, Y.-B., Bach, U. Perovskite tandem solar cells. *Adv Energy Mater* 7, 1602761 (2017).
- 6. Song, Z., Chen, C., Li, C., Awni, R. A., Zhao, D., Yan, Y. Wide-bandgap, low-bandgap, and tandem perovskite solar cells. *Semiconductor Science and Technology* **34**, 093001 (2019).
- 7. Eperon, G. E., *et al.* Perovskite-perovskite tandem photovoltaics with optimized band gaps. *Science* **354**, 861-865 (2016).
- 8. Lin, R., *et al.* Monolithic all-perovskite tandem solar cells with 24.8% efficiency exploiting comproportionation to suppress sn(ii) oxidation in precursor ink. *Nature Energy* **4**, 864-873 (2019).
- 9. Tong, J., *et al.* Carrier lifetimes of >1 μs in sn-pb perovskites enable efficient all-perovskite tandem solar cells. *Science* **364**, 475-479 (2019).
- 10. Chen, B., Zheng, X., Bai, Y., Padture, N. P., Huang, J. Progress in tandem solar cells based on hybrid organic-inorganic perovskites. *Adv Energy Mater* 7, 1602400 (2017).
- 11. Wang, C., Song, Z., Li, C., Zhao, D., Yan, Y. Low bandgap mixed tin lead perovskites and their applications in all perovskite tandem solar cells. *Adv Funct Mater* **29**, 1808801 (2019).
- 12. Zhao, D., *et al.* Efficient two-terminal all-perovskite tandem solar cells enabled by high-quality low-bandgap absorber layers. *Nature Energy* **3**, 1093-1100 (2018).
- 13. Yang, Z., *et al.* Enhancing electron diffusion length in narrow-bandgap perovskites for efficient monolithic perovskite tandem solar cells. *Nat Commun* **10**, 4498 (2019).
- 14. Prasanna, R., *et al.* Design of low bandgap tin–lead halide perovskite solar cells to achieve thermal, atmospheric and operational stability. *Nature Energy* **4**, 939-947 (2019).
- 15. Leijtens, T., *et al.* Tin–lead halide perovskites with improved thermal and air stability for efficient all-perovskite tandem solar cells. *Sustainable Energy & Fuels* **2**, 2450-2459 (2018).
- 16. Kapil, G., *et al.* Strain relaxation and light management in tin–lead perovskite solar cells to achieve high efficiencies. *ACS Energy Letters* **4**, 1991-1998 (2019).
- 17. Forgács, D., *et al.* Efficient monolithic perovskite/perovskite tandem solar cells. *Adv Energy Mater* **7**, 1602121 (2017).
- 18. Wei, M., *et al.* Combining efficiency and stability in mixed tin–lead perovskite solar cells by capping grains with an ultrathin 2d layer. *Adv Mater*, 1907058 (2020).

- 19. Xu, G., *et al.* Integrating ultrathin bulk-heterojunction organic semiconductor intermediary for high-performance low-bandgap perovskite solar cells with low energy loss. *Adv Funct Mater* **28**, 1804427 (2018).
- 20. Liao, W., *et al.* Fabrication of efficient low-bandgap perovskite solar cells by combining formamidinium tin iodide with methylammonium lead iodide. *J Am Chem Soc* **138**, 12360-12363 (2016).
- 21. Zhao, D., *et al.* Low-bandgap mixed tin–lead iodide perovskite absorbers with long carrier lifetimes for all-perovskite tandem solar cells. *Nature Energy* **2**, 17018 (2017).
- 22. Li, C., *et al.* Reducing saturation-current density to realize high-efficiency low-bandgap mixed tin-lead halide perovskite solar cells. *Adv Energy Mater* **9**, 1803135 (2019).
- 23. Li, C., *et al.* Methylammonium-mediated evolution of mixed-organic-cation perovskite thin films: A dynamic composition-tuning process. *Angewandte Chemie* **56**, 7674-7678 (2017).
- 24. Tang, S., *et al.* Composition engineering in doctor-blading of perovskite solar cells. *Adv Energy Mater* 7, 1700302 (2017).
- 25. Yang, M., *et al.* Perovskite ink with wide processing window for scalable high-efficiency solar cells. *Nature Energy* **2**, 17038 (2017).
- 26. Song, Z., *et al.* Probing the origins of photodegradation in organic–inorganic metal halide perovskites with time-resolved mass spectrometry. *Sustainable Energy & Fuels* **2**, 2460-2467 (2018).
- 27. Juarez-Perez, E. J., Ono, L. K., Uriarte, I., Cocinero, E. J., Qi, Y. Degradation mechanism and relative stability of methylammonium halide based perovskites analyzed on the basis of acid-base theory. *ACS Appl Mater Interfaces* **11**, 12586-12593 (2019).
- 28. Lang, F., Shargaieva, O., Brus, V. V., Neitzert, H. C., Rappich, J., Nickel, N. H. Influence of radiation on the properties and the stability of hybrid perovskites. *Adv Mater* **30**, 1702905 (2018).
- 29. Turren-Cruz, S.-H., Hagfeldt, A., Saliba, M. Methylammonium-free, high-performance, and stable perovskite solar cells on a planar architecture. *Science* **362**, 449-453 (2018).
- 30. Prasanna, R., *et al.* Band gap tuning via lattice contraction and octahedral tilting in perovskite materials for photovoltaics. *J Am Chem Soc* **139**, 11117-11124 (2017).
- 31. Yu, Y., *et al.* Improving the performance of formamidinium and cesium lead triiodide perovskite solar cells using lead thiocyanate additives. *ChemSusChem* **9**, 3288-3297 (2016).

- 32. Xu, A. F., Wang, R. T., Yang, L. W., Jarvis, V., Britten, J. F., Xu, G. Pyrrolidinium lead iodide from crystallography: A new perovskite with low bandgap and good water resistance. *Chem Commun* 55, 3251-3253 (2019).
- 33. Fan, J., *et al.* Thermodynamically self-healing 1d-3d hybrid perovskite solar cells. *Adv Energy Mater* **8**, 1703421 (2018).
- 34. Jiang, Q., *et al.* Surface passivation of perovskite film for efficient solar cells. *Nature Photonics* **13**, 460-466 (2019).
- 35. Lian, X., *et al.* Highly efficient sn/pb binary perovskite solar cell via precursor engineering: A two-step fabrication process. *Adv Funct Mater* **29**, 1807024 (2019).
- 36. Jacobsson, T. J., *et al.* Unreacted pbi2 as a double-edged sword for enhancing the performance of perovskite solar cells. *J Am Chem Soc* **138**, 10331-10343 (2016).
- 37. Ogomi, Y., et al. Ch3nh3snxpb(1-x)i3perovskite solar cells covering up to 1060 nm. *J Phys Chem Lett* 5, 1004-1011 (2014).
- 38. Saliba, M., *et al.* Incorporation of rubidium cations into perovskite solar cells improves photovoltaic performance. *Science* **354**, 206-209 (2016).
- 39. Lee, J.-W., Kim, D.-H., Kim, H.-S., Seo, S.-W., Cho, S. M., Park, N.-G. Formamidinium and cesium hybridization for photo- and moisture-stable perovskite solar cell. *Adv Energy Mater* **5**, 1501310 (2015).
- 40. Yi, C., *et al.* Entropic stabilization of mixed a-cation abx3 metal halide perovskites for high performance perovskite solar cells. *Energy Environ Sci* **9**, 656-662 (2016).
- 41. Saliba, M., *et al.* Cesium-containing triple cation perovskite solar cells: Improved stability, reproducibility and high efficiency. *Energy Environ Sci* **9**, 1989-1997 (2016).
- 42. Im, J., Stoumpos, C. C., Jin, H., Freeman, A. J., Kanatzidis, M. G. Antagonism between spinorbit coupling and steric effects causes anomalous band gap evolution in the perovskite photovoltaic materials ch3nh3sn1-xpbxi3. *J Phys Chem Lett* **6**, 3503-3509 (2015).
- 43. Hao, F., Stoumpos, C. C., Chang, R. P., Kanatzidis, M. G. Anomalous band gap behavior in mixed sn and pb perovskites enables broadening of absorption spectrum in solar cells. *J Am Chem Soc* **136**, 8094-8099 (2014).
- 44. Harvey, S. P., Zhang, F., Palmstrom, A., Luther, J. M., Zhu, K., Berry, J. J. Mitigating measurement artifacts in tof-sims analysis of perovskite solar cells. *ACS Appl Mater Interfaces* 11, 30911-30918 (2019).

- 45. Chen, B., Rudd, P. N., Yang, S., Yuan, Y., Huang, J. Imperfections and their passivation in halide perovskite solar cells. *Chemical Society Reviews* **48**, 3842-3867 (2019).
- 46. Yang, W. S., *et al.* Iodide management in formamidinium-lead-halide–based perovskite layers for efficient solar cells. *Science* **356**, 1376-1379 (2017).
- 47. Yin, W.-J., Shi, T., Yan, Y. Unusual defect physics in ch3nh3pbi3 perovskite solar cell absorber. *Appl Phys Lett* **104**, 063903 (2014).
- 48. Wang, C., *et al.* Understanding and eliminating hysteresis for highly efficient planar perovskite solar cells. *Adv Energy Mater* **7**, 1700414 (2017).
- 49. Chen, C., *et al.* Achieving a high open-circuit voltage in inverted wide-bandgap perovskite solar cells with a graded perovskite homojunction. *Nano Energy* **61**, 141-147 (2019).
- 50. Xiao, C., *et al.* Inhomogeneous doping of perovskite materials by dopants from hole-transport layer. *Matter* **2**, 1-12 (2019).
- 51. Khenkin, M. V., et al. Consensus statement for stability assessment and reporting for perovskite photovoltaics based on isos procedures. Nature Energy 5, 35-49 (2020).
- 52. Jackson, W. B., Amer, N. M., Boccara, A. C., Fournier, D. Photothermal deflection spectroscopy and detection. *Appl Opt* **20**, 1333-1344 (1981).